pubs.acs.org/JPCA

Unusually Slow Internal Conversion in N-Heterocyclic Carbene/ Carbanion Cyclometalated Ru(II) Complexes: A Hammett Relationship

- ⁴ William T. Kender and Claudia Turro*
- 5 Department of Chemistry and Biochemistry, The Ohio State University, Columbus, Ohio 43210, United States
- 6 Supporting Information

7

10

11

12

13

14 15

16

17

18

19

20

21

22

23

24

25

26 27

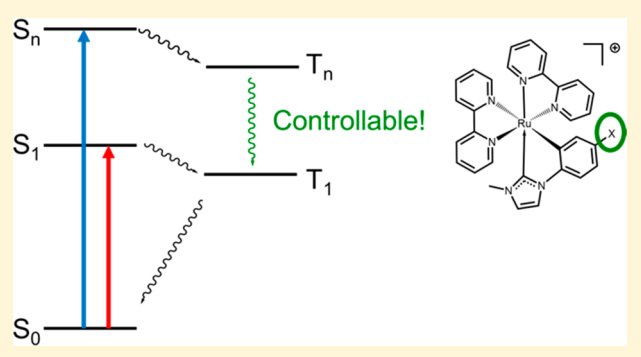
28

29

30

31

ABSTRACT: A series of six $[Ru(bpy)_2(NHC-R)]^+$ complexes were synthesized and characterized, where bpy = 2,2'-bipyridine and NHC-R is an N-heterocyclic carbene covalently linked to a carbanion with a number of substituents, R = -OMe(1), -Me(2), -H(3), -Cl(4), $-CO_2Et(5)$, and $-NO_2(6)$. The effects of these strongly σ -donating NHC-R ligands on the ground-state electronic structure and on the excited-state character and dynamics were probed using electrochemistry, TD-DFT calculations, and steady-state absorption and emission spectroscopies, along with ultrafast transient absorption and time-resolved IR measurements. The excitation of 1-5 with a 400 nm pulse (irf = 85 fs) results in the population of a high energy



singlet state, S_n , that rapidly intersystem crosses into a high-lying triplet state, T_n . Over the course of 7–22 ps, T_n relaxes to the lowest lying triplet state, T_1 , which is metal/ligand-to-ligand charge transfer, ${}^3Ru(d)/NHC(\pi) \rightarrow bpy(\pi^*)$ in character. These 3ML -LCT states decay to regenerate the ground state with lifetimes, τ , that range from <8 to 15 ns at 298 K and from 10 to 23 ns at 77 K in CH₃CN. Both the excited-state lifetime at 77 K and the $T_n \rightarrow T_1$ rate of internal conversion of 1–5 are dependent on the substituent R, and the latter correlates with the Hammett parameter (σ^+_p) of the NHC-R ligand. Excitation of 1–5 with low energy light, 550–670 nm, does not result in the population of T_n , as only T_1 is observed. In the case of 6, excitation is expected to populate a ${}^1Ru(d)/NHC(\pi) \rightarrow NHC(\pi^*)$ state localized on the NHC-NO₂ ligand, which decays to a higher energy ${}^3Ru(d)/NHC(\pi) \rightarrow NHC(\pi^*)$ state followed by internal conversion to the ${}^3Ru(d)/NHC(\pi) \rightarrow bpy(\pi^*)$ T_1 state with $\tau = 250$ ps; the population of both states is independent of excitation wavelength in 6. This work demonstrates that the introduction of one NHC-R ligand in these complexes permits the population of a higher energy triplet state that decays to T_1 in the picosecond time range. The relatively slow $T_n \rightarrow T_1$ internal conversion in these complexes violates Kasha's Law, making the population of the higher-energy state potentially useful for more efficient charge injection into semiconductors for solar energy conversion or to aid in the population of dissociative metal-centered states for drug delivery. Overall, this work shows the ability to synthetically access valuable excited-state dynamics using the two different Ru–C bonds of the asymmetric NHC-R ligands.

33 INTRODUCTION

The excited states of ruthenium polypyridyl complexes have been used extensively in many applications, including photolectrosynthesis cells, 1,2 dye-sensitized solar cells, 5,4 DNA intercalation and sensing, electron transfer reagents, hoton more photon photon photon photon photon intercalation and sensing, electron transfer reagents, hoton more sensing, hoton of the sensing, optoelectronics, and catalysis, sensing, hoton others. Hotology because of the wide range of uses, there has heen great interest in understanding and controlling the excited states of Ru(II) complexes to improve their properties, including lifetime, reactivity, and excitation energy. For example, the steric bulk and bite angle have been shown to have a pronounced effect on the excited-state reactivity and flifetime in Ru(II) complexes, 20,21 and the replacement of nitrogen atoms by isoelectronic carbon, 22 as well as the use of N-heterocyclic carbenes result in marked changes to the excited-state parentage and dynamics. The desirable

properties of Ru(II) complexes can vary from one application 50 to another, such as the requirement of low-lying dissociative 51 metal centered (3MC) states for drug release. 25,26 In contrast, 52 higher energy 3MC states are required to attain longer lifetimes 53 of the lowest energy metal-to-ligand charge transfer (3MLCT) 54 excited state useful for solar energy conversion, sensing, and 55 photoredox catalysis. 27–29 One particular property that may be 56 useful for both areas, enhanced charge injection into 57 semiconductors and increased population of the 3MC state(s) 58 for drug release, is the presence of a 3MLCT state at higher 59 energy that is sufficiently long-lived to afford reactivity.

The Strassner group recently reported cyclometalated 61 ruthenium(II) complexes where there are two Ru–C bonds, 62

Received: January 29, 2019 Revised: March 11, 2019



The Journal of Physical Chemistry A

63 one from a N-heterocyclic carbine and one from a carbanion.³⁰
64 The Nazeeruddin group then introduced a series of electron65 donating and -withdrawing groups on the cyclometallating
66 ligand and showed the profound effect of the substituents on
67 the electrochemistry and on the localization of the frontier
68 molecular orbitals (MOs) on the molecule,³¹ highlighting that
69 the properties of the NHC/carbanion ligand predominantly
70 affect the highest occupied molecular orbital (HOMO) of the
71 molecule, whereas the supporting polypyridyl ligands predom72 inantly affect the lowest unoccupied molecular orbital
73 (LUMO). While the electrochemistry and calculations
74 examined the ground-state molecular orbitals, the excited75 state properties of these complexes were not investigated.

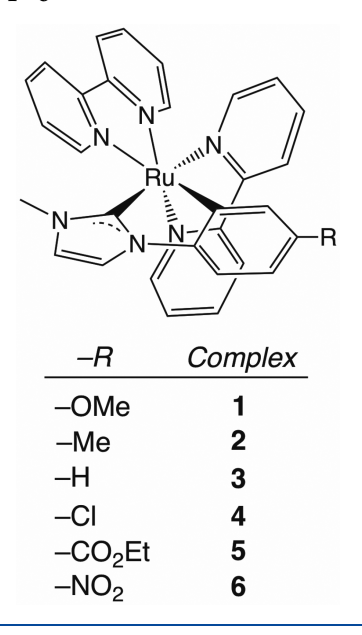
The related cyclometallating ligand 2-phenylpyridine (ppy) 77 was shown to be successful in promoting hole injection from a [Ru(bpy)₂(ppy)]⁺ derivative to a p-type semiconductor, 79 NiO.³² This hole injection is afforded by the covalency 80 between the Ru-C bond of the ppy ligand, such that the 81 HOMO exhibits significant ppy ligand character, resulting in a 82 lowest energy triplet excited state that is $Ru(d)/ppy(\pi) \rightarrow$ 83 bpy (π^*) in character, or meta/ligand-to-ligand charge transfer 84 (3ML-LCT). The delocalization of charge onto the ppy ligand 85 permits efficient hole injection following excitation due to the 86 close spatial proximity between the $Ru(d)/ppy(\pi)$ HOMO 87 and the semiconductor when the ppy ligand is bound to NiO. 88 We hypothesized that the NHC ligands, which bear not only 89 the cyclometallating phenyl group of ppy, but also a highly σ -90 donating carbene lone pair for metal coordination, may exhibit 91 improved excited-state properties as compared to Ru-92 (bpy)₂(ppy)]⁺ for hole injection applications. Importantly, 93 the asymmetry of the NHC ligands is expected to further split 94 the Ru-NHC t_{2g} -type occupied MOs, thus generating two low-95 lying ³ML-LCT states.

The present work focuses on the excited-state properties of 97 six complexes with the general formula [Ru(bpy)₂(NHC-98 R)][PF₆], where bpy = 2.2'-bipyridine and NHC-R represent 99 an N-heterocyclic carbene covalently bound to a deprotonated 100 phenyl ring with a substituent -R positioned para to the NHC 101 moiety. In the $Ru(bpy)_2(NHC-R)[PF_6]$ series, R = -OMe102 (1), -Me(2), -H(3), -Cl(4), $-\text{CO}_2\text{Et}(5)$, and $-\text{NO}_2(6)$, 103 as depicted in Scheme 1. The Hammett parameters (σ_p^+) of 104 the NHC-R ligands in 1-6 vary widely from -0.78 to 0.79 and 105 range from electron-donating to electron-withdrawing. Com-106 plexes 1-6 exhibit extensive mixing of Ru and the NHC-R 107 ligand in the HOMO. Two low-lying triplet excited states, T_n 108 and T₁, are observed, both of which exhibit sufficiently long 109 lifetimes to afford hole injection into NiO. While two 110 independent low-lying ³MLCT states have been previously 111 observed for Ru(II) complexes, 33,34 to the best of our 112 knowledge, this represents the first report of the population 113 of two triplet states with sufficiently slow $T_n \rightarrow T_1$ internal 114 conversion in a cyclometalated or in a carbene complex to 115 afford reactivity from both states.

116 EXPERIMENTAL SECTION

Materials. The synthesis of complexes 1, 30 3, 4,30 and 6 30 118 was accomplished following methods previously described, 119 while 2, 4, and 5 were prepared using modified versions of the 120 same published routes. The syntheses of the NHC-R ligands 121 for 2, 35 4, 36 and 5 37 have been previously described. The 122 solvents, as well as 2,2'-bipyridine, ammonium hexafluor-123 ophosphate, tetra-"butyl ammonium hexafluorophosphate, and 124 cesium carbonate, were purchased from Sigma-Aldrich. The

Scheme 1. Schematic Representation of the Molecular Structures of 1-6



details of the synthesis are described in the Supporting 125 Information and shown in Scheme S1 along with NMR and 126 mass spectrometry data in Figures S1—S10.

Instrumentation and Methods. ¹H NMR spectra were 128 obtained on a either a 400 or a 250 MHz Bruker DPX 129 spectrometer (as noted in the Supporting Information) and 130 referenced to the residual solvent peaks, 7.26 ppm for CDCl₃- 131 d_1 and 1.94 ppm for CD₃CN- d_3 . Electrospray ionization was 132 performed on a Bruker MicrOTOF mass spectrometer, and 133 samples were dissolved in acetonitrile and standardized with 134 sodium formate in water. Steady-state UV-vis electronic 135 absorption data were collected on an Agilent Cary 8453 diode 136 array spectrometer with a 1 cm × 1 cm quartz cuvette 137 equipped with a gastight Kontes screwtop. Emission data were 138 recorded on a FluoroMax-4 spectrofluorimeter (Horiba Jobin 139 Yvon) in CH₃CN, and samples were deareated by sparging 140 with nitrogen for 15 min. The solutions were loaded into J- 141 Young tubes and cooled with liquid nitrogen. Steady-state 142 infrared absorption data were measured on a Spectrum 65 FT- 143 IR spectrometer by PerkinElmer. The sample was contained 144 within an airtight Herrick sample cell equipped with two 1 mm 145 CaF₂ plates and a 0.1 mm spacer.

Time-resolved femtosecond transient absorption (fsTA) 147 spectroscopy data were collected on a system that was 148 previously described in detail.³⁹ Briefly, an Astrella laser 149 system (Coherent) is used to provide an 800 nm pulse (8 mJ, 150 1 kHz rep. rate, ~35 fs pulse width). The Ti:Saph output was 151 split to serve as the pump beam (3 mJ) and the remainder as 152 the probe pulse. The excitation pulses pump an optical 153 parametric amplifier (Coherent OPerA Solo), and the output 154 was directed through an optical delay line (maximum delay of 155 4 ns) and attenuated to 2 μ J. All samples were at a 156 concentration that afforded an absorption of $\sim 0.3-0.5$ at the 157 sample excitation wavelength. A supercontinuum of white light 158 was generated by focusing a portion of the remaining 800 nm 159 beam onto a CaF2 window on a rotating mount. The resulting 160 light was dispersed on a Triax 550 spectrograph before being 161 detected by a PIXIS CCD camera (Princeton Instruments) run 162 using a home-built LabView program. The temporal resolution 163

164 or instrument response function (irf) was 85 fs determined 165 from the measurement of the optical Kerr effect in cyclo-166 hexane. The samples were flowed in a Herrick Scientific flow 167 cell, which features two 1 mm CaF₂ plates with a 1 mm spacer. Femtosecond time-resolved infrared spectroscopy (TRIR) 169 was also conducted on an instrument previously described in 170 detail.⁴⁰ Briefly, a Legend (Coherent) was seeded by a Mantis 171 (Coherent) short pulse oscillator with 800 nm output (2.4 mJ, 172 1 kHz rep. rate), and the output was split and directed into two 173 different optical parametric amplifiers (OPerA, Coherent). 174 One of the OPerA outputs was passed through an optical delay 175 line and served as the pump (maximum delay of 3 ns), while 176 the other was equipped with a difference frequency generation 177 module, which created the mid-IR continuum and served as 178 the probe beam. The sample cell used for TRIR was the same 179 as that for the steady-state IR experiments, and the absorption 180 of each sample at the pump wavelength was adjusted to be 181 between 0.5-0.8. The mid-IR light was dispersed by a Triax 182 320 spectrograph and detected using a HgCdTe CCD chip (32 183 × 2 pixels) with ~4 cm⁻¹ resolution (InfraRed Associates 184 Inc.). The 180 fs time resolution was determined by measuring 185 the growth of the ${}^{3}MLCT$ signature of $[Ru(bpy)_{3}][PF_{6}]_{2}$.

The electronic absorption spectrum of each sample was measured before and after each time-resolved experiment to lss ensure that no sample degradation had taken place. Addition-ls9 ally, for all femtosecond time scale measurements, the pump beams were passed through a linear polarizer set to the magic angle of between the probe and pump beams to minimize the measurements of anisotropy. All kinetic traces from fsTA and TRIR were plotted and fitted using the Igor Pro software (version 6.3.4.1) with a sum of exponential equations.

Transient absorption spectroscopy in the nanosecond time scale (nsTA) was performed on an instrument previously described. Briefly, an Edinburgh LP980 spectrometer sequipped with single-wavelength photomultiplier tube detector and an intensified CCD camera was used for broadband measurement. The third harmonic of a Spectra-Physcis INDI-201 40 Nd:YAG laser (100 mJ/pulse, 10 Hz rep. rate) was focused onto a Spectra-Physics Basiscan optical parametric oscillator to produce the wavelengths of light used for excitation, attenuated to $\sim 6-8$ mJ/pulse for the experiments. The samples were deaerated and loaded into the cells used for steady-state deectronic absorption at an absorption of ~ 0.3 at the excitation wavelength.

Cyclic voltammograms (CVs) were recorded under a N₂ 209 atmosphere using a BASi CV-50W (Bioanalytical Systems Inc.) 210 potentiostat. The cell consisted of a three-electrode arrange-211 ment with a glassy carbon disc working electrode, a Ag/AgCl 212 aqueous working electrode (3 M NaCl), and a platinum coil 213 counter-electrode. All CVs were measured at a 20 mV/s scan ²¹⁴ rate in CH₃CN with 0.1 M tetra-"BuNPF₆ as the electrolyte ²¹⁵ and referenced to the Fc^{+/0} couple ($E_{1/2}$ = +0.382 V vs SCE) 216 by adding ferrocene to the sample cell following each 217 experiment. 44 The same potentiostat and reference electrode 218 were used for the spectroelectrochemical measurements, with a 219 glassy carbon rod as the working electrode and a carbon fiber 220 mesh as the counter-electrode to increase the surface area in 221 contact with the solution. The two-compartment cell was 222 connected by a porous frit and continuously bubbled with 223 nitrogen, and the transmission side was fabricated using a 1 \times 224 1 cm quartz cuvette. The potentials of 1-5 were held 200 mV 225 more positive than the oxidation $E_{1/2}$ and 200 mV more 226 negative than the reduction $E_{1/2}$ to record the absorption spectra of the one-electron oxidized and reduced species, 227 respectively. Complex 6 was held at 100 mV past the reduction 228 potential to prevent overlap with the second reduction peak. 229 The potentials were held until the current flow decreased by 230 95% of the initial value.

A Bruker D8 Venture Photon II with CPAD was used to 232 collect the single-crystal X-ray diffraction data for all four 233 complexes. The crystals were cooled with a stream of cold N₂ 234 to 150 K with an Oxford Cryosystems Cryostream Cooler. 235 These structures were then solved using the OLEX program 236 with a plugin using the SHELXT program, which used an 237 intrinsic phasing solution method. 2,45,46 The resulting data 238 were processed using SHELXL, which used a full-matrix least- 239 squares/difference Fourier cycle treatment for refinements. 47 240 All non-hydrogen atoms were refined with anisotropic 241 displacement parameters. Most hydrogen atoms were placed 242 in ideal positions and refined as riding atoms with relative 243 isotropic displacement parameters, but in some instances using 244 the residual electron density map to assign hydrogen peaks 245 gave significantly better results. These hydrogen atoms are 246 identified and additional information is provided in the 247 Supporting Information.

Complexes 3 and 6 have been previously characterized by 249 single-crystal X-ray crystallography. 30,31 Although 1 was 250 reported previously, it was not characterized crystallographi- 251 cally, and 2, 4, and 5 are new molecules. All of crystallographic 252 data for these complexes are provided in the Supporting 253 Information. Crystals for 1 and 2 were grown with the slow 254 diffusion of hexanes into a concentrated solution of acetone, 255 and those of 4 and 5 were grown in an analogous manner but 256 with acetonitrile and diethyl ether. For the crystal structure of 257 5, there was a large solvent channel that was the approximate 258 length of two diethyl ether molecules. As such, we attempted 259 to model the channel with two Et₂O molecules, both with 260 positional disordered over multiple positions, but this resulted 261 in a poor fit. These solvent molecules were removed using 262 PLATON, function: SQUEEZE, which resulted in the removal 263 of 144 electrons and a 479 Å³ solvent-accessible void per cell 264 (consistent with two diethyl ether molecules). For complexes 4 265 and 5, one PF₆⁻ counteranion in each structure exhibited 266 positional disorder. These were modeled by splitting the 267 disordered atoms into groups (PART instruction), moving the 268 atoms to the expected positions on the basis of residual 269 electron density, and allowing the atoms to refine freely. This 270 method was also used to model the positional disorder in 1 271 and 2 for the acetone molecules present in the crystal 272

All computational results were obtained using the Guassian 274 09 suite of programs. 48 For geometry optimization and 275 frequency calculations (both singlet and triplet), the PBE 276 hybrid functional was used as it resulted in the best match with 277 experimental data. 49 The frequency calculations confirmed that 278 the calculated structures were at a local minima. For time- 279 dependent DFT,50 the B3LYP functional was found to best 280 reproduce the experimental data.⁵¹ For all calculations, the ²⁸¹ def2-TZVP basis set^{52,53} was used for all atoms^{4,41} with the 282 exception of ruthenium where the use of SDD ab initio 283 pseudopotentials was employed. 54,55 All of the calculations 284 were undertaken using a Polarizable Continuum Model 285 (PCM)⁵⁶ with CH₃CN as the solvent. Natural bonding orbital 286 (NBO) calculations were undertaken to quantify the 287 percentage contribution of ruthenium-based orbitals to 288 molecular orbitals.

290 RESULTS AND DISCUSSION

Synthesis and Single-Crystal X-ray Crystallographic Characterization. Complexes 1, 3, and 6 were previously synthesized following the steps depicted in Scheme S1, 30,31 whereas 2, 4, and 5 were new and were prepared following an analogous procedure. Complexes 1–6 were recrystallized from slow diffusion of diethyl ether into a concentrated acetonitrile solution, and the single-crystal X-ray diffraction structures of 1, 298 2, 4, and 5 are shown in Figure 1. There is very little

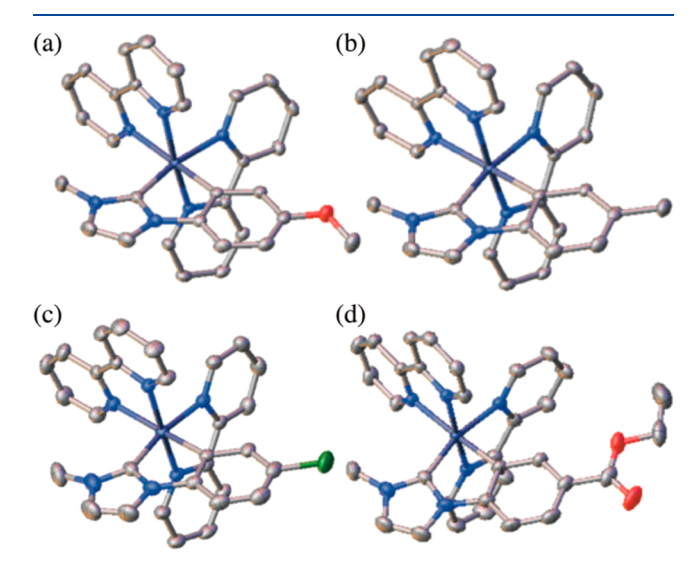


Figure 1. Thermal ellipsoid plots of (a) **1**, (b) **2**, (c) **4**, and (d) **5** shown at 50% probability (gray = carbon, blue = nitrogen, red = oxygen, green = chlorine, and dark blue = ruthenium); crystallized solvent molecules, counteranions, and hydrogens are omitted for clarity.

299 perturbation across the four complexes in the $\sim 101^{\circ}$ C–Ru–C 300 angles, with the largest difference of 0.5°, or in the Ru–C 301 distances, where the largest difference is 0.02 Å. The Ru–C 302 distances in 1, 2, 4, and 5 are comparable to those reported for 303 [Ru(bpy)₂(ppy)]⁺ and related cyclometalated complexes, 304 which feature bond lengths in the 1.99–2.08 Å range. The 305 atomic coordinates and crystallographic details specific to each 306 crystal are summarized in Tables S1–S8.

Electronic Absorption, Emission, and Electrochemis-308 try. The room-temperature electronic absorption and 77 K 309 emission spectra of 1–6 in CH₃CN are shown in Figure 2, and

f2t1

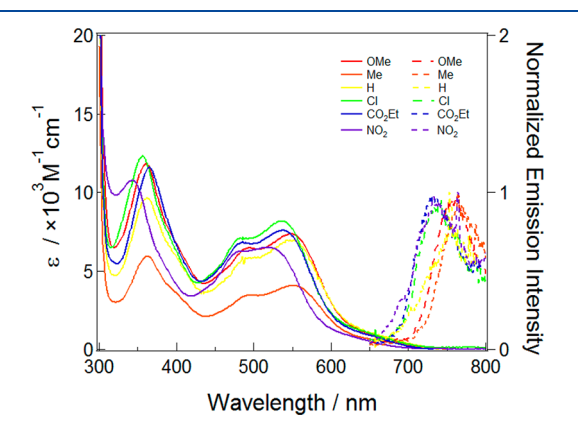


Figure 2. Electronic absorption (solid lines, 298 K) and emission (dashed lines, $\lambda_{\rm exc} = 540$ nm, 77 K) of 1-6 in CH₃CN.

relevant data are summarized in Table 1. Complex 1 exhibits a 310 tl ligand-centered ${}^{1}\pi\pi^{*}$ transition associated with the NHC-OMe 311

Table 1. Electronic Absorption Maxima, λ_{abs} , Molar Extinction Coefficients, ε , and Electrochemical Reduction Potentials, $E_{1/2}$, for 1–6 in CH₃CN

complex	$\lambda_{\rm abs}/{\rm nm}~(\varepsilon/{\rm \times}10^3~{\rm M}^{-1}~{\rm cm}^{-1})$	$E_{1/2}/V^a$		
1	360 (12), 494 (6.5), 548 (7.4)	-1.50, +0.50		
2	363 (5.9), 492 (3.4), 550 (4.1)	-1.48, +0.51		
3	363 (9.6), 488 (5.5), 547 (7.0)	-1.49, +0.52		
4	357 (12), 485 (7.0), 537 (8.2)	-1.48, +0.60		
5	364 (12), 486 (6.9), 539 (7.6)	-1.49, +0.58		
6	344 (11), 482 (6.2), 519 (6.5)	-1.52, -1.34 , -1.12 , $+0.69$		
^a 0.1 M Bu₄NPF ₆ ; vs Ag/AgCl.				

ligand at 360 nm and two singlet metal/ligand-to-ligand charge 312 transfer (1 ML-LCT) bands with maxima at 493 and 549 nm; 313 the latter tails from \sim 620 to \sim 750 nm. Complexes **2**–**6** exhibit 314 similar features that resemble the electronic absorption 315 spectrum of $[Ru(bpy)_{2}(ppy)]^{+}$, with maxima at 365, 402, 316 486, and 543 nm in methanol. The series features a 317 bathochromic shift of the 1 ML-LCT peaks from **6** at 519 nm 318 to **1** at 548 nm as the NHC-R ligand becomes more electron-319 donating, making the Ru(II) center easier to oxidize.

As shown in Figure 2, 1 emits light with maximum at 763 321 nm ($\lambda_{\rm exc}$ = 540 nm) in CH₃CN at 77 K with a large Stokes 322 shift (5060 cm⁻¹) from the lowest energy ¹ML-LCT peak at 323 549 nm, consistent with the luminescence of related Ru(II) 324 complexes. 60,61 Similar phosphorescence is observed for 2-6 325 at 77 K (Figure 2). These features are common among all six 326 complexes; the maxima of 1-3 appear at roughly the same 327 energy, ~760 nm, and those of 4-6 at ~735 nm. Emission at 328 room temperature was not detected for 1-6 in CH₃CN. The 329 low emission is in contrast to $[Ru(bpy)_3]^{2+}$, which absorbs at 330 452 nm and emits at room temperature ($\lambda_{em} = 620 \text{ nm}$). 62 It is 331 expected that the increase in σ -donating ability of the NHC-R 332 ligand should result in an increase in energy of the metal- 333 centered highest occupied molecular orbital (HOMO), thus 334 lowering the energy required to promote an electron into the 335 bpy(π^*) LUMO. This red shift in the absorption observed for 336 1-6 is also present in $[Ru(bpy)_2(ppy)]^+$ relative to that of 337 $[Ru(bpy)_3]^{2+.59}$

The electrochemistry of 1-6 was examined in acetonitrile, 339 and the results are shown in Figure 3 and summarized in Table 340 f3 1. The first oxidation of 1 is observed at $E_{1/2} = +0.50 \text{ V vs Ag}/341$ AgCl in CH₃CN, and it shifts to more positive potentials with 342 increasing electron-withdrawing ability of the substituent on 343 the NHC-R ligand; the magnitude of the difference between 344 the first oxidation in 1 and 6 is 190 mV, and that between 3 345 and 6 is 170 mV. This couple is assigned to a metal-centered 346 oxidation, and the shift is comparable to that measured for 347 $[Ru(bpy)_2(ppy)]^+$ and $[Ru(bpy)_2(NO_2-ppy)]^+$, where NO_2 - 348 ppy is a NO₂-substituted phenylpyridine, +120 mV.⁵⁸ For 349 complexes 1-5, the first reduction couple is essentially 350 unchanged, within ~20 mV, and is assigned to the reduction 351 of the bpy ligand. Similar complexes with only bpy ligands 352 feature their first ligand reductions at roughly this poten- 353 tial. 63-65 However, 6 exhibits a positive shift of 380 mV 354 attributed to the stabilization of the π^* orbital of the NHC- 355 NO₂/carbanion orbital by the presence of the strong electron- 356 withdrawing group.

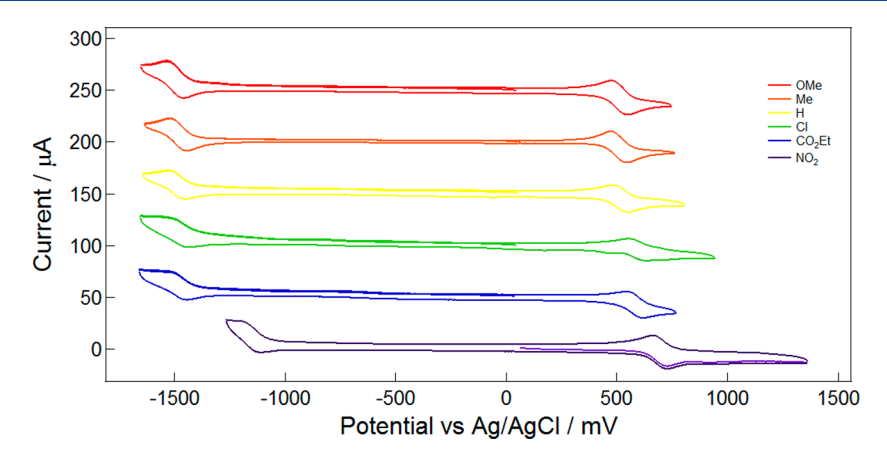


Figure 3. Cyclic voltammograms of 1-6 recorded in CH₃CN (0.1 M "Bu₄NPF₆ electrolyte; each trace above complex 6 is offset by 50 μ A for clarity).

Density Functional Theory Calculations. The calculated molecular orbital (MO) diagrams of 1–6 are shown in Figure 4, which display a clear trend in the energy of the HOMO

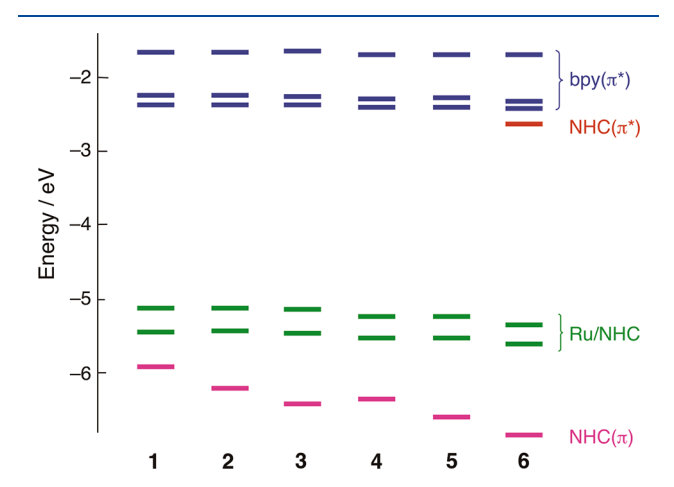


Figure 4. Ground-state singlet molecular orbital diagrams for 1-6.

361 across the series. The HOMO of the complex with the most electron-donating NHC-R ligand (R = -OMe), 1, is slightly destabilized as compared to that with a -H substituent, 3. The 364 opposite trend is calculated for 6, where the HOMO is stabilized relatively those of 1-5. The calculated HOMO 366 energy difference of 0.24 eV from 1−6 is in reasonably good 367 agreement with the electrochemistry data, which show a total 368 shift in the first oxidation couple of 0.19 V from 1 to 6. The 369 calculated energies of the LUMOs of 1-5 are also in good 370 agreement with the electrochemical data, with only a small difference of <30 meV among the five complexes and 372 consistent with an MO centered on a bpy(π^*) orbital. In contrast, a large difference in the energy of the LUMO is 373 calculated for 6, 220 meV, as compared to the next closest in 375 value, 5. This finding is consistent with the electrochemisty 376 and also with the calculated localization of the LUMO on the 377 NHC-NO₂(π^*) orbital positioned at a lower energy than the 378 bpy(π^*) MOs (Figure 4).

The absorption data generally agree with the trends found in 380 the DFT and TD-DFT calculations (Tables S9–S14). The 381 electron-donating NHC-OMe ligand in 1 raises the energy of 382 the HOMO as compared to the rest of the series, resulting in a 383 smaller HOMO-LUMO gap reflected in the red-shifted

lowest energy absorption maximum for this complex. The 384 tails of absorption are difficult to compare due to their low 385 intensity, but these too appear to agree with the calculated 386 values, because those of complexes with more electron- 387 donating ligands extend further into the red wavelengths and 388 with a higher intensity as compared to those with electron- 389 withdrawing groups.

The electron densities of the frontier molecular orbitals of 391 1-5 are similar and exemplified in the electron density plots 392 shown in Figure 5 for 2. The contribution from the 393 fs

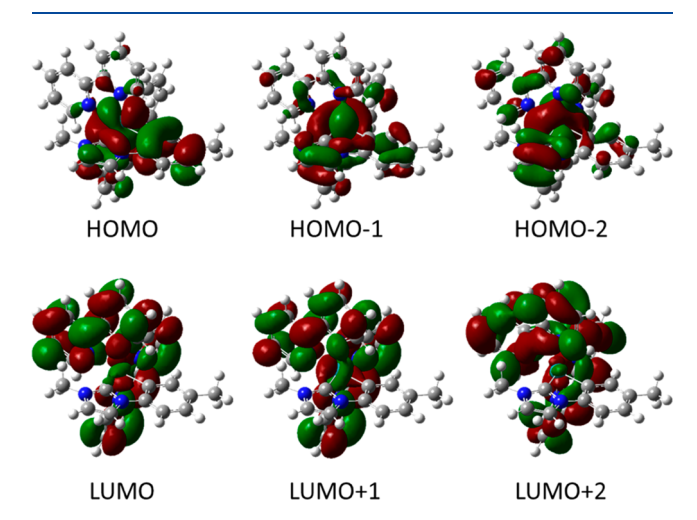


Figure 5. Electron density plots of the frontier MOs of 2 (drawn at isovalue = 0.02).

cyclometallating ligand is clearly evident in the HOMO, 394 HOMO-1, and HOMO-2 of **2**. In contrast, the LUMO, 395 LUMO+1, and LUMO+2 of **2** exhibit nearly no contribution 396 from the NHC/carbanion ligand, with the majority of the 397 electron density residing on the bpy ligands. In complex **6**, the 398 LUMO is NHC-NO $_2(\pi^*)$ in character below the bpy(π^*) 399 orbitals. The electron density of the LUMO of **6** is depicted in 400 Figure S15. These trends are consistent with the NBO 401 calculation results, summarized in Tables S15 and S16, where a 402 greater contribution to the HOMO is calculated for the more 403 electron-donating ligands, as evidenced by a decrease in total 404 Ru contribution.

The TD-DFT calculations predict a large number of low 406 oscillator strength bands at lower energies for 1-6, the lowest 407

408 of which arises primarily from the HOMO → LUMO 409 transition. Together with the experimental data and compar-410 isons to related complexes, the computational results lead to an 411 assignment of the lowest energy absorption in 1-5 as arising 412 from the population of the lowest energy singlet, ¹ES₁, 413 associated with a Ru(d)/NHC(π) \rightarrow bpy(π *) transition of 1 ML-LCT character, and a ligand-centered Ru(d)/NHC(π) \rightarrow 415 NHC(π^*) transition for 6. The singlet excited states 416 immediately above ¹ES₁, ¹ES₂-¹ES₄, are calculated to possess 417 relatively low oscillator strengths, with the next transition with significant intensity predicted to be to ¹ES₅, and primarily 419 composed of electron density movement from the HOMO-1 420 and HOMO-2 to the LUMO+1 and LUMO+2. The 421 HOMO-1 and HOMO-2 are localized on the NHC-R 422 ligand and the Ru metal, but possess significantly smaller 423 contribution from the carbanion ring as compared to the 424 HOMO. The ${}^{1}GS_{1} \rightarrow {}^{1}ES_{5}$ transition is predicted at 519 nm in 425 1 and is calculated to progressively shift to higher energy across 426 the series to 507 nm in 5. These results are in qualitative 427 agreement with the electronic absorption data for the 428 complexes in Figure 2 and Table 1. The lowest energy triplet 429 excited state of each of 1-6 is predicted to be ³ML-LCT in 430 nature (Figures S16-S20).

Spectroelectrochemistry and Nanosecond Transient 432 **Absorption.** The spectroelectrochemistry of 1-6 was utilized 433 to aid in the interpretation of the transient absorption data. 434 Upon oxidation of 1-6, a decrease in the absorption in the 435 400-600 nm range is observed, along with a broad increase in 436 intensity at ~600 nm. In similar Ru(III) polypyridyl 437 complexes, the absorption at long wavelengths has been 438 previously attributed to ligand-to-metal charge transfer 439 (LMCT) transitions from ligand(π) to Ru³⁺(d) orbitals, 440 while the decrease in ground-state absorption is associated 441 with a shift in the MLCT transition to higher energies outside 442 the measurement window. 41,66,67 The difference spectra 443 collected upon one-electron reduction are similar for 1-5, 444 but substantially different for complex 6, as expected from the 445 electrochemistry and DFT calculations. Reduction of 1-5 446 results in an increased absorption in the UV and near-UV 447 regions, indicating the presence of a reduced bpy ligand, 68 448 whereas in the case of 6, the one-electron reduced complex 449 absorbs strongly from 350-450 nm and beyond 550 nm 450 (Figure S25). These features are attributed to the reduction of 451 the NHC/carbanion ligand rather than the modest increases in 452 the UV region typical of bpy radical anions. These changes are exemplified in difference absorption plots in Figure 6a for the oxidation and reduction of 5.

The nanosecond transient absorption spectra of 1-5 exhibit 456 broadband absorption profiles that bear a striking resemblance 457 to the spectroelectrochemistry data, as shown in Figure 6b for 458 5. A ground-state bleach is observed in 1-5 between 400-600 459 nm, and broad positive absorption features at λ < 400 nm and 460 between 600 and 800 nm, consistent with a ³ML-LCT excited state. In general, the decays of both the positive signal and the 462 bleach can be fitted to a monoexponential function consistent 463 with the relaxation of the ³ML-LCT excited state to the ground state with $\tau = 15 \pm 0.1$ ns (Table 2). The instrument response 465 function (irf) of the instrument is \sim 8 ns, and the lifetimes, τ , of 466 some of the complexes cannot be accurately deconvoluted 467 from the irf; in fact, **1–6** exhibit τ < 20 ns at room temperature 468 and are summarized in Table 2. As expected, extension of the 469 3ML-LCT lifetimes was observed for 1-6 at 77 K, and the 470 results are listed in Table 2 for 1-5. On this instrument, the

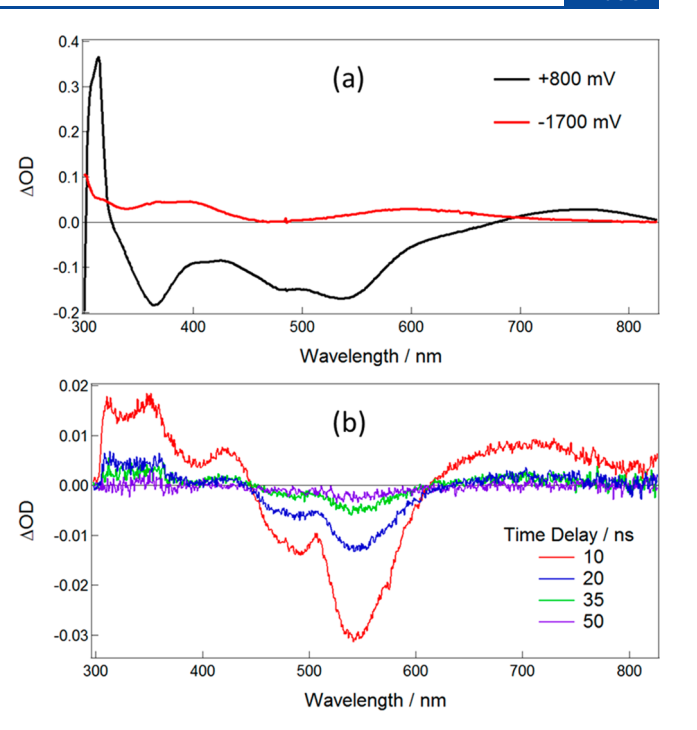


Figure 6. Difference spectra of **5** (a) recorded after electrochemical oxidation and reduction at +0.8 and -1.7 V vs Ag/AgCl, respectively, and (b) collected at various times following a 550 nm excitation (irf ~ 6 ns) in deaerated CH₃CN.

Table 2. Excited-State Lifetimes of 1-5 in CH₃CN

complex	τ/ps^a	τ/ns^c	τ/ns^d
1	7 ± 2	3-8	10.1 ± 0.1
2	9 ± 1	3-8	10.1 ± 0.3
3	10 ± 3^{b}	8.7 ± 0.3	11.3 ± 0.3
4	16 ± 2	15.9 ± 0.1	16.2 ± 0.1
5	22 ± 3^{b}	15.2 ± 0.1	23.0 ± 0.1

^aA long-lived component with $\tau > 3$ ns was observed for 1–5; $\lambda_{\rm exc} = 400$ nm, irf ~85 fs. ^bA <1.0 ps vibrational cooling component was observed. ^c $\lambda_{\rm exc} = 550-670$ nm, 298 K, irf ~8 ns. ^d $\lambda_{\rm exc} = 550$ nm, 77 K, irf ~8 ns, fit to the decay of emission.

lifetime of **6** at 298 K was too short to be observed, but was 471 measured to be 9.9 \pm 0.1 ns at 77 K in CH₃CN ($\lambda_{\rm exc}$ = 550 472 nm).

Femtosecond Transient Absorption and Time-Re- 474 solved IR (TRIR) Spectroscopies. To elucidate the excited- 475 state dynamics of 1-6, each of the complexes was examined 476 using pump-probe spectroscopy on the femtosecond time 477 scale. When complex 1 is excited in the 550-670 nm range, a 478 large ground-state bleach between 450 and 600 nm develops 479 within the laser pulse (Figures 7 and S24). Additionally, a 480 f7 small but persistent excited-state absorption is observed at 481 wavelengths >600 nm, consistent a ³ML-LCT excited state. 482 With these low energy excitation wavelengths, only a 483 vibrational cooling component is observed along with signal 484 that does not decay within the 3 ns maximum time scale of 485 measurement. Similar spectral and decay profiles were 486 collected for 2-5 (Figures S25-S29), and these results are 487 consistent with the >3 ns lifetimes observed using nanosecond 488 excitation (Table 2).

With 400 nm excitation, higher energy excited states are 490 accessed, leading to an additional component in the pico- 491 second time range for 1-5 as summarized in Table 2 and 492

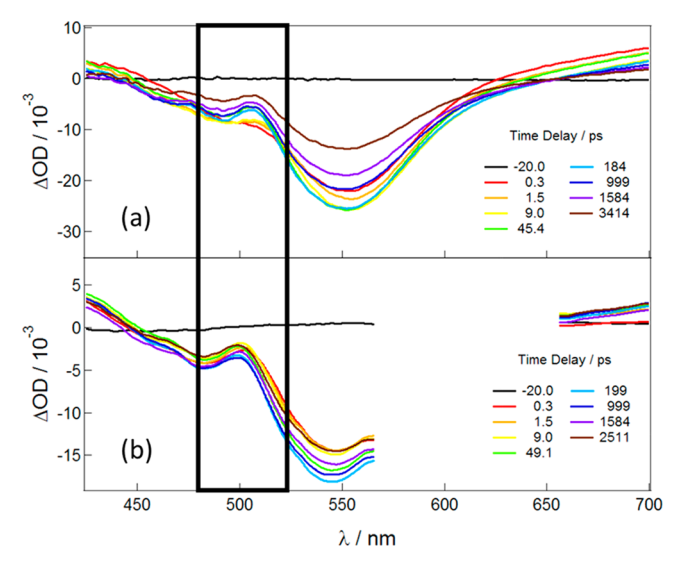


Figure 7. Transient absorption spectra of 1 in CH_3CN at various delay times following (a) 400 nm and (b) 620 nm excitation (irf = 85 fs). The black box highlights the spectral differences between the two excitation wavelengths.

493 exemplified in Figure 7a for 1. This 7–22 ps component is 494 evident in the growth of a feature at ~510 nm for 1–5 during 495 this time range (Figure 7a for 1 and Figures S25–S29 for 2–496 5). At longer wavelengths, a shift is also observed at roughly 497 the same time scale. This shift and the spectral changes at 498 ~510 are not observed with lower energy excitation of 1–5. 499 In Ru(II) complexes, intersystem crossing (ISC) is known to 500 proceed within ~40 fs, 69,70 such that the differences observed 501 with 400 nm and 550–670 nm excitation in the picosecond 502 time scale must be taking place in the triplet manifold. In 503 general, the spectral features of the 7–22 ps component in 1–504 5 are similar to those of the long-lived excited state with $\tau \ge 3$

ns, such that they can both be assigned as arising from 3ML - 505 LCT states. It may be hypothesized that ISC upon 400 nm 506 excitation results in the initial population of a higher energy 507 1ML -LCT state that intersystem crosses to a higher energy 508 triplet 3ML -LCT state, T_n , within the 85 fs laser pulse; the 509 latter then decays to the lowest energy 3ML -LCT state, T_1 , 510 with time constants that range from 7–22 ps in 1–5 (Table 2). 511 Population of the lowest energy 1ML -LCT state of 1–5 with 512 550–670 nm excitation results in the observation of the 3ML - 513 LCT T_1 state, which decays to the ground state with lifetimes 514 \geq 3 ns, as listed in Table 2.

To gain further information on the population of the 3 ML- $_{516}$ LCT 7 L state, complex 1 L was pumped using different 517 Wavelengths, 400, 550, 620, 640, and 670 nm; however, only 518 400 nm excitation gave rise to the 7 ps component (Figure 7a). 519 There was not a substantial difference observed in the longer 520 Wavelength excitations. Complexes 2 —5 were examined with a 521 Minimum of three pump wavelengths, 400, 550, and 670 s22 (Figures 525 —S29). Similar to the results for 1 , the component 523 With lifetime in the 9 - 22 ps range was only observed with 400 s24 nm, and there was no significant difference in band shape or 525 lifetime between 550 nm and 850 nm.

In contrast to 1–5, the transient absorption signals observed 527 for 6 exhibit a biexponential decay regardless of excitation at 528 high or low energy from 400 to 670 nm, with $\tau_1 = 90 \pm 30$ ps 529 (47%) and $\tau_2 = 180 \pm 50$ ps (53%) in CH₃CN at 298 K ($\lambda_{\rm exc} = 530$ 400 nm, fit at 591 nm). From the calculations, the lowest 531 energy singlet transition in 6 is predicted to be $^1{\rm Ru}({\rm d})/532$ NHC(π) \rightarrow NHC(π^*) in nature, whereas the lowest energy 533 minimized structure of the triplet state is $^3{\rm Ru}({\rm d})/{\rm NHC}(\pi) \rightarrow 534$ bpy(π^*). As such, the transient absorption experiments can be 535 explained by the initial population of the $^1{\rm Ru}({\rm d})/{\rm NHC}(\pi) \rightarrow 536$ NHC(π^*) state upon absorption of a photon, followed by 537 intersystem crossing to both a higher energy $^3{\rm Ru}({\rm d})/{\rm NHC}(\pi) \rightarrow 538$ \rightarrow NHC(π^*) state, $T_{\rm n}$, and the lowest energy $^3{\rm Ru}({\rm d})/539$ NHC(π) \rightarrow bpy(π^*) state, $T_{\rm 1}$. The assignment of both states 540

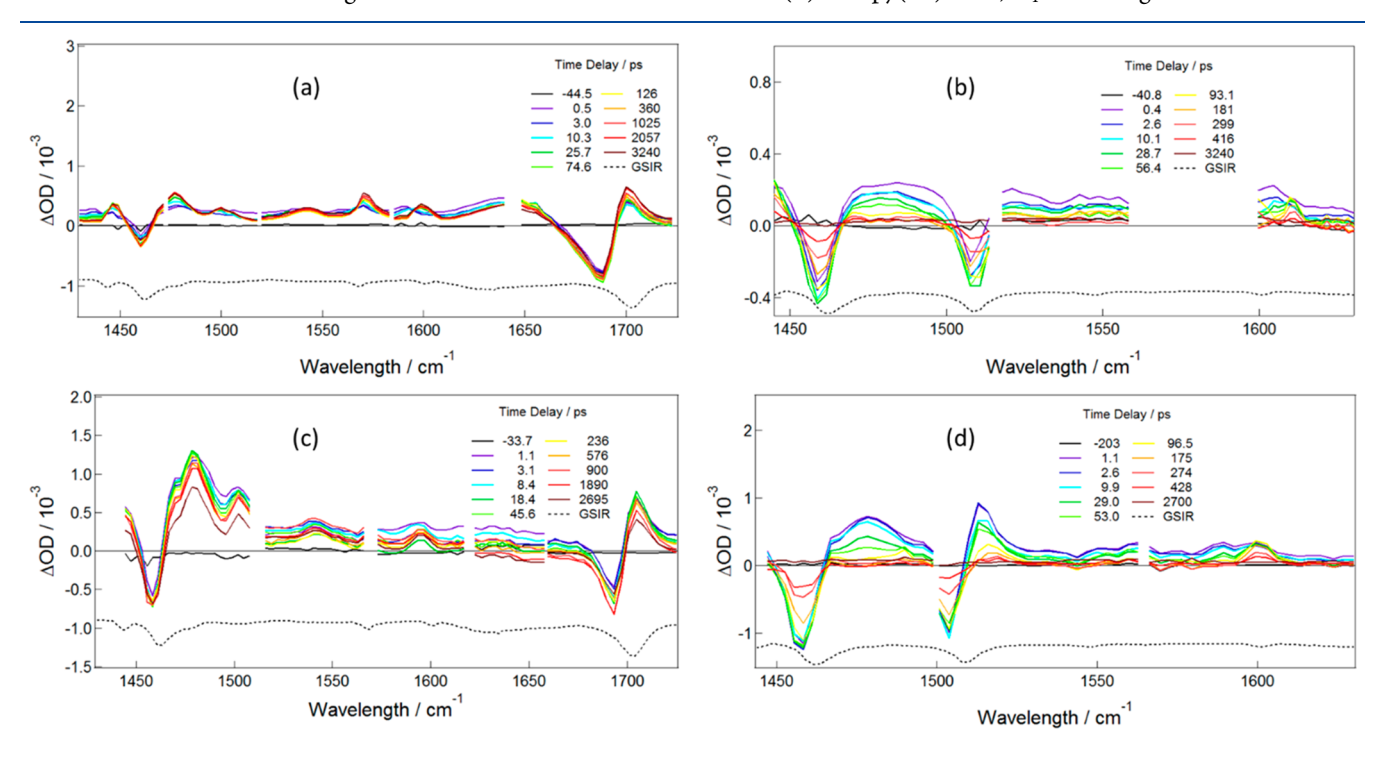


Figure 8. TRIR difference spectra in acetonitrile- d_3 of (a,c) 5 and (b,d) 6 with (a,b) $\lambda_{\rm exc} = 400$ nm and (c,d) 6 $\lambda_{\rm ex} = 585$ nm (irf ~185 fs).

The Journal of Physical Chemistry A

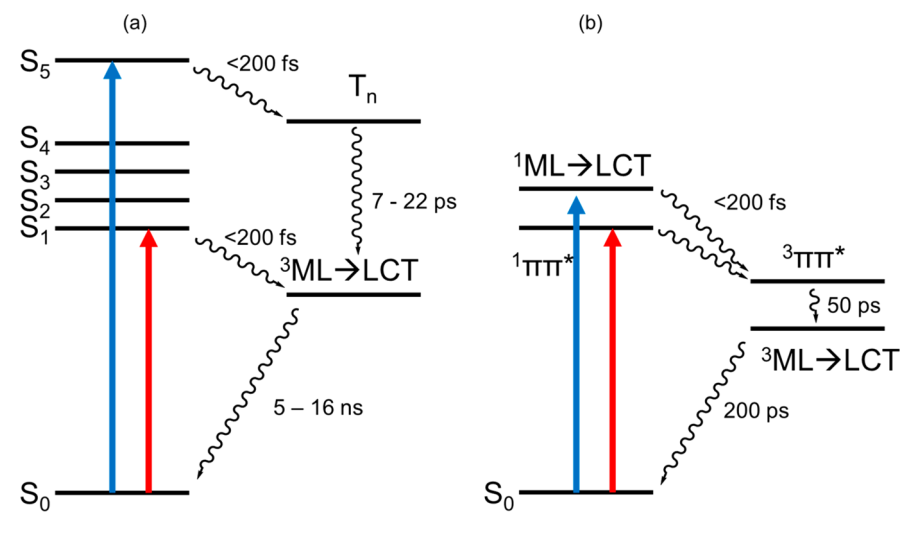


Figure 9. Jablonski diagrams of the excited-state processes in (a) 1–5 and (b) 6 where a $Ru(d)/NHC(\pi) \rightarrow NHC(\pi^*)$ state is denoted as $\pi\pi^*$ and a $Ru(d)/NHC(\pi) \rightarrow bpy(\pi^*)$ state is denoted as $ML \rightarrow LCT$.

541 as 3 ML-LCT in **6** stems from the similarities to those of **1–5**. 542 Moreover, the $T_n \rightarrow T_1$ transition in **6** features changes at 543 \sim 510 nm, as is also the case for **1–5**.

To further examine the spectral features of the triplet T_n state of 1–6, TRIR spectroscopy was employed using multiple s46 pump wavelengths in CD₃CN (irf ~185 fs). Complexes 5 and 547 6, which have IR specific markers, were examined in the ~1400 s48 to ~1700 cm⁻¹ range to capture any shifts of both of the ligand s49 aromatic ring stretches and the IR active functional groups, s50 whereas 1–4 were only monitored between ~1420 and 1550 s51 cm⁻¹.

Each complex was excited with 400 nm pump light and a 552 553 lower energy pump wavelength that corresponded to the red side of the absorption maximum (Figure 8 and Figures S30-S33). With higher energy excitation of 5, several features grow 556 in over the course of 25 ps (Figure 8a). Most notably, a new peak develops at 1500 cm⁻¹, and the peak corresponding to the 558 aromatic ring stretch at 1590 cm⁻¹ shifts to higher energy by 559 10 cm⁻¹. The time scale of these changes, 22 ps, is consistent s60 with the decay of the higher-energy ³ML-LCT state, T_n, to T₁ 561 measured by fsTA (Table 2). The changes are not consistent 562 with vibrational relaxation usually observed in TRIR spectra, 563 which are signified by the sharpening of peaks without 564 significant shifting or growth. These changes are not observed 565 in the spectra collected with a lower energy pump (Figure 8c), 566 consistent with the absence of the picosecond decay for 1-5. 567 When excited with shorter wavelength light, the observed shift 568 of the aromatic peak to higher frequencies is explained by a 569 loss of back-donation from the Ru(II) to π^* orbitals on the 570 NHC ligand when the metal is oxidized in the charge transfer state.⁷¹ Notably, there is no shift in the CO₂Et IR handle at 1700 cm⁻¹, which reflects the lack of a rearrangement of electron density on that portion of the ligand. These observations parallel those measured in the transient absorption and point to a $T_n \rightarrow T_1$ internal conversion with time constant of 22–25 ps from a higher ³ML-LCT state to the lowest ${}^{3}ML$ -LCT state. The kinetics of the $T_n \rightarrow T_1$ transition measured in the TRIR experiments are consistent with those 579 recorded in the transient absorption measurements of 1-4 580 (Figures S20-S23).

Unlike 1-5, there are no differences upon excitation of 6 s82 with 400 and 550 nm (Figure 8b and d). In each case, the

vibrational frequency of the -NO2 group is observed to shift 583 from 1595 cm⁻¹ at early times to 1610 cm⁻¹ at late times. The 584 lifetime associated with this shift, 50 ± 20 ps, is consistent with 585 the measured transient absorption data. The early time points 586 of the spectra show the -NO₂ band at lower frequencies than 587 the ground-state frequency (1602 cm⁻¹). This is consistent 588 with a removal of electron density from a bonding orbital and 589 placing it into an antibonding orbital as in a $Ru(d)/NHC(\pi)$ 590 \rightarrow NHC(π^*) state. At later times, this band moves to higher 591 frequencies, indicating an increased bond strength. The 592 calculations predict that a higher stretching frequency would 593 result in the ${}^{3}\text{Ru}(d)/\text{NHC}(\pi) \rightarrow \text{bpy}(\pi^{*})$ exited state of 6 as 594 compared to the ground state by \sim 7 cm⁻¹, which is consistent 595 with the experimentally observed values. The TRIR of 6, as is 596 also the case with the fsTA experiments, can be explained by 597 the initial population of the ${}^{1}Ru(d)/NHC(\pi) \rightarrow NHC(\pi^{*})$ 598 state upon absorption of a photon, followed by intersystem 599 crossing to both a higher energy ${}^{3}\text{Ru}(d)/\text{NHC}(\pi) \rightarrow {}_{600}$ NHC(π^*) state and the lowest energy ${}^3\text{Ru}(d)/\text{NHC}(\pi) \rightarrow 601$ bpy(π^*), T₁.

These results show that the excitation of 1–5 with low $_{603}$ energy light results in the population of the lowest energy $_{604}$ $^1\text{ML-LCT}$ state, which directly converts to the lowest energy $_{605}$ $^3\text{ML-LCT}$ state, T_1 , before returning to the ground state. With $_{606}$ high energy light, the initial population of S_n affords $_{607}$ intersystem crossing to T_n , which then undergoes internal $_{608}$ conversion to the lowest energy $^3\text{ML-LCT}$ state, T_1 . This $_{609}$ pathway is shown in Figure 9a, where the $T_n \rightarrow T_1$ internal $_{610}$ $_{609}$ conversion takes place with time constants of 7–22 ps in 1–5. $_{611}$ In complex 6, both high- and low-energy excitation result in $_{612}$ the initial population of the $_{38}^3\text{Ru}(d)/\text{NHC}(\pi) \rightarrow _{38}^3\text{NHC}(\pi^*)$ $_{613}^3$ state, such that internal conversion in the triplet manifold is $_{614}^3$ present and independent of excitation wavelength (Figure 9b). $_{615}^3$

Relationship of Hammett Parameter to Excited-State 616 Deactivation. The trend of the time constant of the $T_n \rightarrow T_1$ 617 for 1-5 can be correlated to a Hammett parameter within the 618 series. Complex 6 is excluded from this analysis because the 619 excited-state dynamics likely involve $\pi\pi^*$ states, which are 620 inaccessible to the other complexes. While this series is small, 621 there is a clear trend that arises from the picosecond lifetimes 622 measured in both the fsTA and the fsTRIR data. The more 623 electron-donating substituents lead to a shorter initial lifetime, 624

669

685

625 7 ± 2 ps for R = -OMe in 1, and more electron-withdrawing 626 substituents lead to a longer lifetime, 22 ± 3 ps for $R = 627 - CO_2Et$ in 5.

When fit to a Hammett parameter plot, the short lifetimes 629 measured from fsTA data fit best with the σ_p^+ para parameters 630 that have been optimized for electron donation into a π -631 electron-accepting system (such as a Ru³⁺ center),⁷² as shown 632 in Figure 10 ($R^2 = 0.97$). The linear fit when using the σ_p^+

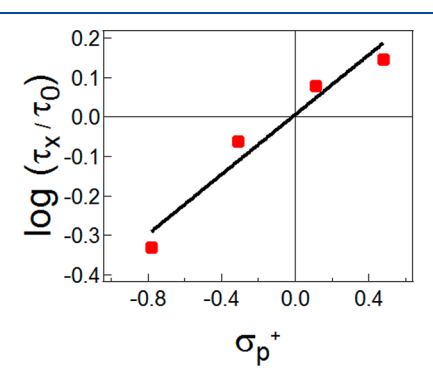


Figure 10. A Hammett parameter plot of the rates of internal conversion from $T_n \to T_1$ in 1, 2, 4, and 5 as a function of σ_p^+ values, where τ_x is the lifetime of T_n for each complex and τ_0 is the lifetime of T_n for complex 3.

633 parameters shows that the rearrangement of electron density 634 on the ruthenium center is not the primary effect that controls 635 the $T_n \to T_1$ rate constant, which is positioned meta to the 636 substituent R in NHC-R, and would result in a better fit with 637 σ_m values. Instead, the movement of electron density on the 638 NHC ligand appears to be more important in controlling this 639 process, where the substitutent is *para* to the carbene-640 containing NHC ring. While not conclusive by itself, this 641 analysis is consistent with the assignment of a T_n state that is 642 Ru³⁺ based, but with significant unpaired electron density in 643 the NHC/carbanion ligand in the ³ML-LCT excited state(s).

644 CONCLUSION

645 The six ruthenium cyclometalated/carbene complexes of the 646 type [Ru(bpy)₂(NHC-R)]⁺ exhibit low-energy light absorption 647 and have unique and controllable excited-state dynamics. In 648 each of the complexes, there are two low-energy triplet states 649 that are Ru(d)/NHC(π) \rightarrow bpy(π *) 3 ML-LCT in nature. The 650 rate of internal conversion from the higher energy triplet, T_n, 651 to T₁ is controlled by an easily modifiable substituent R on the 652 NHC-R ligand, which exhibits significant covalency to the 653 Ru(II) metal center. For each of the six complexes, the two 654 states, T_n and T₁, are sufficiently long-lived to undergo charge 655 injection into a semiconductor following excitation with visible 656 light. Because the hole of the HOMO extends onto the 657 synthetically modifiable NHC-R ligand, these complexes have 658 the potential to be capable hole-injectors into p-type 659 semiconductors for use in solar energy conversion devices. 660 Using a Hammett parameter analysis, deeper understanding 661 into the nature of these excited states can be gained ,and 662 general guiding principles for excited-state engineering in these 663 complexes are established. Importantly, the ability of the 664 NHC-R complexes to populate a higher energy excited state 665 with an appreciable lifetime provides a means to improve not 666 only charge injection but can also play a role in enhancing the 667 population of higher-lying metal-centered state(s) important 668 for photoinduced drug delivery.

ASSOCIATED CONTENT

Supporting Information

The Supporting Information is available free of charge on the 671 ACS Publications website at DOI: 10.1021/acs.jpca.9b00858. 672

Synthetic schemes, characterization data, mass spec- 673 trometry, NMR, X-ray crystallography data, additional 674 DFT and TD-DFT information, and additional nsTA, 675 fsTA, fsTRIR, and spectroelectrochemistry spectra 676 (PDF)

AUTHOR INFORMATION

AUTHOR INFORMATION	67
Corresponding Author	67
E-mail: turro.1@osu.edu.	68
ORCID [®]	68
Claudia Turro: 0000-0003-3202-5870	68
Notes	68
The authors declare no competing financial interest.	68

ACKNOWLEDGMENTS

We would like to thank the National Science Foundation 686 (CHE-1800395) for partial support of this work, as well as Dr. 687 Judy Galluci and Dr. Malik Al-Afyouni for their assistance with 688 the collection and processing of the crystal structure data.

REFERENCES

I

- (1) Brennaman, M. K.; Dillon, R. J.; Alibabaei, L.; Gish, M. K.; 691 Dares, C. J.; Ashford, D. L.; House, R. L.; Meyer, G. J.; Papanikolas, J. 692 M.; Meyer, T. J. Finding the Way to Solar Fuels with Dye-Sensitized 693 Photoelectrosynthesis Cells. *J. Am. Chem. Soc.* **2016**, *138*, 13085—694 13102.
- (2) Song, W.; Vannucci, A. K.; Farnum, B. H.; Lapides, A. M.; 696 Brennaman, M. K.; Kalanyan, B.; Alibabaei, L.; Concepcion, J. J.; 697 Losego, M. D.; Parsons, G. N.; et al. Visible Light Driven Benzyl 698 Alcohol Dehydrogenation in a Dye-Sensitized Photoelectrosynthesis 699 Cell. J. Am. Chem. Soc. 2014, 136, 9773—9779.
- (3) Grätzel, M. Dye-Sensitized Solar Cells. J. Photochem. Photobiol., 701 C 2003, 4, 145–153.
- (4) Aghazada, S.; Nazeeruddin, M. K. Ruthenium Complexes as 703 Sensitizers in Dye-Sensitized Solar Cells. *Inorganics* **2018**, *6*, 52.
- (5) Swierk, J. R.; Regan, K. P.; Jiang, J.; Brudvig, G. W.; 705 Schmuttenmaer, C. A. Rutile TiO₂ as an Anode Material for Water- 706 Splitting Dye-Sensitized Photoelectrochemical Cells. *ACS Energy Lett.* 707 **2016**, *1*, 603–606.
- (6) Aghazada, S.; Ren, Y.; Wang, P.; Nazeeruddin, M. K. Effect of 709 Donor Groups on the Performance of Cyclometalated Ruthenium 710 Sensitizers in Dye-Sensitized Solar Cells. *Inorg. Chem.* **2017**, *56*, 711 13437—13445.
- (7) Keane, P. M.; Kelly, J. M. Transient Absorption and Time- 713 Resolved Vibrational Studies of Photophysical and Photochemical 714 Processes in DNA-Intercalating Polypyridyl Metal Complexes or 715 Cationic Porphyrins. *Coord. Chem. Rev.* **2018**, *364*, 137–154.
- (8) Lennox, J. C.; Kurtz, D. A.; Huang, T.; Dempsey, J. L. Excited- 717 State Proton-Coupled Electron Transfer: Different Avenues for 718 Promoting Proton/Electron Movement with Solar Photons. ACS 719 Energy Lett. 2017, 2, 1246–1256.
- (9) Ji, S.; Wu, W.; Wu, W.; Guo, H.; Zhao, J. Ruthenium(II) 721 Polyimine Complexes with a Long-Lived ³IL Excited State or a 722 ³MLCT/³IL Equilibrium: Efficient Triplet Sensitizers for Low-Power 723 Upconversion. *Angew. Chem.* **2011**, 123, 1664–1667.
- (10) Ji, S.; Guo, H.; Wu, W.; Wu, W.; Zhao, J. Ruthenium(II) 725 Polyimine—Coumarin Dyad with Non-Emissive ³IL Excited State as 726 Sensitizer for Triplet—Triplet Annihilation Based Upconversion. 727 Angew. Chem. **2011**, 123, 8433–8436.

- 729 (11) Bolze, F.; Jenni, S.; Sour, A.; Heitz, V. Molecular Photo-730 sensitisers for Two-Photon Photodynamic Therapy. *Chem. Commun.* 731 **2017**, 53, 12857–12877.
- 732 (12) Jin, Y.; Harrington, D.; Rachford, A. A.; Rack, J. J. Stimulating 733 Changes in the Elastic Modulus of Polymer Materials by Molecular 734 Photochromism. *RSC Adv.* **2014**, *4*, 62920–62925.
- 735 (13) Vos, J. G.; Kelly, J. M. Ruthenium Polypyridyl Chemistry; from 736 Basic Research to Applications and Back Again. *Dalton Trans.* **2006**, 737 41, 4869–4883.
- 738 (14) Basha, S. S.; Sundari, G. S.; Kumar, K. V.; Rao, K. R.; Rao, M. 739 C. Preparation and Characterization of Ruthenium Based Organic 740 Composites for Optoelectronic Device Application. *Optik* **2018**, *164*, 741 596–605.
- 742 (15) Prier, C. K.; Rankic, D. A.; MacMillan, D. W. C. Visible Light 743 Photoredox Catalysis with Transition Metal Complexes: Applications 744 in Organic Synthesis. *Chem. Rev.* **2013**, *113*, 5322–5363.
- 745 (16) R. Gill, M.; A. Thomas, J. Ruthenium(II) Polypyridyl 746 Complexes and DNA—from Structural Probes to Cellular Imaging 747 and Therapeutics. *Chem. Soc. Rev.* **2012**, *41*, 3179–3192.
- 748 (17) Zakeeruddin, S. M.; Nazeeruddin, M. K.; Humphry-Baker, R.; 749 Péchy, P.; Quagliotto, P.; Barolo, C.; Viscardi, G.; Grätzel, M. Design, 750 Synthesis, and Application of Amphiphilic Ruthenium Polypyridyl 751 Photosensitizers in Solar Cells Based on Nanocrystalline TiO₂ Films. 752 *Langmuir* **2002**, *18*, 952–954.
- 753 (18) Balzani, V.; Juris, A. Photochemistry and Photophysics of 754 Ru(II)-polypyridine Complexes in the Bologna Group. From Early 755 Studies to Recent Developments. *Coord. Chem. Rev.* **2001**, 211, 97–756 115.
- 757 (19) Hammarström, L. Accumulative Charge Separation for Solar 758 Fuels Production: Coupling Light-Induced Single Electron Transfer 759 to Multielectron Catalysis. *Acc. Chem. Res.* **2015**, *48*, 840–850.
- 760 (20) Damrauer, N. H.; Boussie, T. R.; Devenney, M.; McCusker, J. 761 K. Effects of Intraligand Electron Delocalization, Steric Tuning, and 762 Excited-State Vibronic Coupling on the Photophysics of Aryl-763 Substituted Bipyridyl Complexes of Ru(II). *J. Am. Chem. Soc.* 1997, 764 119, 8253–8268.
- 765 (21) Breivogel, A.; Meister, M.; Förster, C.; Laquai, F.; Heinze, K. 766 Excited State Tuning of Bis(tridentate) Ruthenium(II) Polypyridine 767 Chromophores by Push—Pull Effects and Bite Angle Optimization: A 768 Comprehensive Experimental and Theoretical Study. *Chem. Eur. J.* 769 **2013**, *19*, 13745—13760.
- 770 (22) Constable, E. C.; Housecroft, C. E. The Electronic Structure of 771 Some Ruthenium(II) Complexes Related to $[Ru(bipy)_3]^{2+}$: An 772 Investigation of the Stepwise Replacement of N,N-Donors by C,N-773 Donors. *Polyhedron* **1990**, *9*, 1939–1947.
- 774 (23) Park, H.-J.; Kim, K. H.; Choi, S. Y.; Kim, H.-M.; Lee, W. I.; 775 Kang, Y. K.; Chung, Y. K. Unsymmetric Ru(II) Complexes with N-776 Heterocyclic Carbene and/or Terpyridine Ligands: Synthesis, 777 Characterization, Ground- and Excited-State Electronic Structures 778 and Their Application for DSSC Sensitizers. *Inorg. Chem.* 2010, 49, 779 7340–7352.
- 780 (24) D. Ertl, C.; P. Ris, D.; C. Meier, S.; C. Constable, E.; E. 781 Housecroft, C.; Neuburger, M.; A. Zampese, J. Sticking and Patching: 782 Tuning and Anchoring Cyclometallated Ruthenium(II) Complexes. 783 *Dalton Trans.* **2015**, *44*, 1557–1570.
- 784 (25) Knoll, J. D.; Turro, C. Control and Utilization of Ruthenium 785 and Rhodium Metal Complex Excited States for Photoactivated 786 Cancer Therapy. *Coord. Chem. Rev.* **2015**, 282, 110–126.
- 787 (26) Wagenknecht, P. S.; Ford, P. C. Metal Centered Ligand Field 788 Excited States: Their Roles in the Design and Performance of 789 Transition Metal Based Photochemical Molecular Devices. *Coord.* 790 *Chem. Rev.* **2011**, 255, 591–616.
- 791 (27) Brown, D. G.; Sanguantrakun, N.; Schulze, B.; Schubert, U. S.; 792 Berlinguette, C. P. Bis(tridentate) Ruthenium—Terpyridine Com-793 plexes Featuring Microsecond Excited-State Lifetimes. *J. Am. Chem.* 794 Soc. **2012**, 134, 12354–12357.
- 795 (28) Bomben, P. G.; Robson, K. C. D.; Koivisto, B. D.; Berlinguette, 796 C. P. Cyclometalated Ruthenium Chromophores for the Dye-797 Sensitized Solar Cell. *Coord. Chem. Rev.* **2012**, 256, 1438–1450.

- (29) Parada, G. A.; Fredin, L. A.; Santoni, M.-P.; Jäger, M.; Lomoth, 798 R.; Hammarström, L.; Johansson, O.; Persson, P.; Ott, S. Tuning the 799 Electronics of Bis(tridentate)ruthenium(II) Complexes with Long- 800 Lived Excited States: Modifications to the Ligand Skeleton beyond 801 Classical Electron Donor or Electron Withdrawing Group Deco- 802 rations. *Inorg. Chem.* 2013, 52, 5128–5137.
- (30) Schleicher, D.; Leopold, H.; Borrmann, H.; Strassner, T. 804 Ruthenium(II) Bipyridyl Complexes with Cyclometalated NHC 805 Ligands. *Inorg. Chem.* **2017**, *56*, 7217–7229.
- (31) Aghazada, S.; Zimmermann, I.; Scutelnic, V.; Nazeeruddin, M. 807 K. Synthesis and Photophysical Characterization of Cyclometalated 808 Ruthenium Complexes with N-Heterocyclic Carbene Ligands. 809 Organometallics 2017, 36, 2397—2403.
- (32) Ji, Z.; Natu, G.; Huang, Z.; Kokhan, O.; Zhang, X.; Wu, Y. 811 Synthesis, Photophysics, and Photovoltaic Studies of Ruthenium 812 Cyclometalated Complexes as Sensitizers for P-Type NiO Dye- 813 Sensitized Solar Cells. *J. Phys. Chem. C* 2012, 116, 16854–16863. 814
- (33) Sun, Y.; Liu, Y.; Turro, C. Ultrafast Dynamics of the Low-Lying 815

 ³MLCT States of [Ru(bpy)₂(dppp2)]²⁺. *J. Am. Chem. Soc.* **2010**, 132, 816

 5594–5595.
- (34) Sun, Y.; Turro, C. Highly Solvent Dependent Luminescence 818 from $[Ru(bpy)_n(dppp2)_{3-n}]^{2+}$ (n = 0-2). *Inorg. Chem.* **2010**, 49, 819 5025-5032.
- (35) Unger, Y.; Meyer, D.; Molt, O.; Schildknecht, C.; Münster, I.; 821 Wagenblast, G.; Strassner, T. Green−Blue Emitters: NHC-Based 822 Cyclometalated [Pt(C∧C*)(acac)] Complexes. *Angew. Chem., Int. Ed.* 823 **2010**, 49, 10214−10216.
- (36) Tronnier, A.; Poethig, A.; Herdtweck, E.; Strassner, T. $C \land C^*$ 825 Cyclometalated Platinum(II) NHC Complexes with β -Ketoimine 826 Ligands. *Organometallics* **2014**, 33, 898–908.
- (37) Fuertes, S.; Chueca, A. J.; Perálvarez, M.; Borja, P.; Torrell, M.; 828 Carreras, J.; Sicilia, V. White Light Emission from Planar Remote 829 Phosphor Based on NHC Cycloplatinated Complexes. ACS Appl. 830 Mater. Interfaces 2016, 8, 16160–16169.
- (38) Fulmer, G. R.; Miller, A. J. M.; Sherden, N. H.; Gottlieb, H. E.; 832 Nudelman, A.; Stoltz, B. M.; Bercaw, J. E.; Goldberg, K. I. NMR 833 Chemical Shifts of Trace Impurities: Common Laboratory Solvents, 834 Organics, and Gases in Deuterated Solvents Relevant to the 835 Organometallic Chemist. Organometallics 2010, 29, 2176–2179.
- (39) Burdzinski, G.; Hackett, J. C.; Wang, J.; Gustafson, T. L.; 837 Hadad, C. M.; Platz, M. S. Early Events in the Photochemistry of Aryl 838 Azides from Femtosecond UV/Vis Spectroscopy and Quantum 839 Chemical Calculations. *J. Am. Chem. Soc.* 2006, 128, 13402–13411. 840 (40) Wang, J.; Burdzinski, G.; Kubicki, J.; Gustafson, T. L.; Platz, M. 841 S. Ultrafast Carbene–Carbene Isomerization. *J. Am. Chem. Soc.* 2008, 842 130. 5418–5419.
- (41) Henry, W.; Coates, C. G.; Brady, C.; Ronayne, K. L.; Matousek, 844 P.; Towrie, M.; Botchway, S. W.; Parker, A. W.; Vos, J. G.; Browne, 845 W. R.; et al. The Early Picosecond Photophysics of Ru(II) Polypyridyl 846 Complexes: A Tale of Two Timescales. *J. Phys. Chem. A* **2008**, *112*, 847 4537–4544.
- (42) Stark, C. W.; Schreier, W. J.; Lucon, J.; Edwards, E.; Douglas, 849 T.; Kohler, B. Interligand Electron Transfer in Heteroleptic 850 Ruthenium(II) Complexes Occurs on Multiple Time Scales. *J. Phys.* 851 Chem. A 2015, 119, 4813–4824.
- (43) Whittemore, T. J.; White, T. A.; Turro, C. New Ligand Design 853 Provides Delocalization and Promotes Strong Absorption throughout 854 the Visible Region in a Ru(II) Complex. *J. Am. Chem. Soc.* **2018**, *140*, 855 229–234.
- (44) Aranzaes, J. R.; Daniel, M.-C.; Astruc, D. Metallocenes as 857 References for the Determination of Redox Potentials by Cyclic 858 Voltammetry Permethylated Iron and Cobalt Sandwich Complexes, 859 Inhibition by Polyamine Dendrimers, and the Role of Hydroxy- 860 Containing Ferrocenes. *Can. J. Chem.* **2006**, 84, 288–299.
- (45) Dolomanov, O. V.; Bourhis, L. J.; Gildea, R. J.; Howard, J. a. K.; 862 Puschmann, H. OLEX2: A Complete Structure Solution, Refinement 863 and Analysis Program. *J. Appl. Crystallogr.* **2009**, 42, 339–341.

The Journal of Physical Chemistry A

- 865 (46) Sheldrick, G. M. SHELXT Integrated Space-Group and 866 Crystal-Structure Determination. *Acta Crystallogr., Sect. A: Found. Adv.* 867 **2015**, 71, 3–8.
- 868 (47) Sheldrick, G. M. Crystal Structure Refinement with SHELXL. 869 Acta Crystallogr., Sect. C: Struct. Chem. 2015, 71, 3–8.
- 870 (48) Frisch, M. J.; Trucks, G. W.; Schlegel, H. B.; Scuseria, G. E.; 871 Robb, M. A.; Cheeseman, J. R.; Scalmani, G.; Barone, V.; Petersson,
- 872 G. A.; Nakatsuji, H.; et al. *Gaussian 09*, revision E.01; Gaussian, Inc.: 873 Wallingford, CT, 2016.
- 874 (49) Perdew, J. P.; Burke, K.; Ernzerhof, M. Generalized Gradient 875 Approximation Made Simple. *Phys. Rev. Lett.* **1996**, 77, 3865–3868.
- 376 (50) Runge, E.; Gross, E. K. U. Density-Functional Theory for Time-Dependent Systems. *Phys. Rev. Lett.* **1984**, *52*, 997–1000.
- 878 (51) Becke, A. D. Density-functional Thermochemistry. III. The
- 879 Role of Exact Exchange. *J. Chem. Phys.* **1993**, 98, 5648–5652. 880 (52) Weigend, F.; Ahlrichs, R. Balanced Basis Sets of Split Valence,
- 881 Triple Zeta Valence and Quadruple Zeta Valence Quality for H to Rn: 882 Design and Assessment of Accuracy. *Phys. Chem. Chem. Phys.* **2005**, *7*, 883 3297—3305.
- 884 (53) Weigend, F. Accurate Coulomb-Fitting Basis Sets for H to Rn. 885 Phys. Chem. Chem. Phys. **2006**, 8, 1057–1065.
- 886 (54) Andrae, D.; Häußermann, U.; Dolg, M.; Stoll, H.; Preuß, H. 887 Energy-Adjusted Ab Initio Pseudopotentials for the Second and Third 888 Row Transition Elements. *Theor. Chim. Acta* **1990**, *77*, 123–141.
- 889 (55) Andrae, D.; Häußermann, U.; Dolg, M.; Stoll, H.; Preuß, H. 890 Energy-Adjusted Ab Initio Pseudopotentials for the Second and Third 891 Row Transition Elements: Molecular Test for M2 (M = Ag, Au) and 892 MH (M = Ru, Os). *Theor. Chim. Acta* **1991**, 78, 247–266.
- 893 (56) Cancès, E.; Mennucci, B.; Tomasi, J. A New Integral Equation 894 Formalism for the Polarizable Continuum Model: Theoretical 895 Background and Applications to Isotropic and Anisotropic Dielectrics. 896 J. Chem. Phys. 1997, 107, 3032–3041.
- 897 (57) Glendening, E. D.; Reed, A. E.; Carpenter, J. E.; Weinhold, F. 898 NBO Version 3.1.
- 899 (58) Reveco, P.; Schmehl, R. H.; Cherry, W. R.; Fronczek, F. R.; 900 Selbin, J. Cyclometalated Complexes of Ruthenium. 2. Spectral and 901 Electrochemical Properties and X-Ray Structure of bis(2,2'-
- 902 bipyridine)(4-Nitro-2-(2-pyridyl)phenyl)ruthenium(II). *Inorg. Chem.* 903 1985, 24, 4078–4082.
- 904 (59) Constable, E. C.; Holmes, J. M. A Cyclometallated Analogue of 905 Tris(2,2'-bipyridine)ruthenium(II). *J. Organomet. Chem.* **1986**, 301, 906 203–208.
- 907 (60) Bouskila, A.; Drahi, B.; Amouyal, E.; Sasaki, I.; Gaudemer, A. 908 Mononuclear and Binuclear Ruthenium(II) Heteroleptic Complexes 909 Based on 1,10-Phenanthroline Ligands: Part I: Synthesis, Spectro-910 scopic and Photophysical Study. *J. Photochem. Photobiol., A* **2004**, *163*, 911 381–388.
- 912 (61) Evans, R. C.; Douglas, P.; Winscom, C. J. Coordination 913 Complexes Exhibiting Room-Temperature Phosphorescence: Evalua-914 tion of Their Suitability as Triplet Emitters in Organic Light Emitting 915 Diodes. *Coord. Chem. Rev.* **2006**, *250*, 2093–2126.
- 916 (62) Kalyanasundaram, K. Photophysics, Photochemistry and Solar 917 Energy Conversion with Tris(bipyridyl)ruthenium(II) and its 918 Analogues. *Coord. Chem. Rev.* 1982, 46, 159–244.
- 919 (63) Pavlishchuk, V. V.; Addison, A. W. Conversion Constants for 920 Redox Potentials Measured versus Different Reference Electrodes in
- 921 Acetonitrile Solutions at 25°C. *Inorg. Chim. Acta* **2000**, 298, 97–102.
- 922 (64) Tokel-Takvoryan, N. E.; Hemingway, R. E.; Bard, A. J. 923 Electrogenerated Chemiluminescence. XIII. Electrochemical and
- 923 Electrogenerated Chemiluminescence. XIII. Electrochemical and 924 Electrogenerated Chemiluminescence Studies of Ruthenium Chelates.
- 925 J. Am. Chem. Soc. 1973, 95, 6582-6589.
- 926 (65) Saji, T.; Aoyagui, S. Polarographic Studies on Bipyridine 927 Complexes: I. Correlation between Reduction Potentials of Iron(II),
- 928 Ruthenium(II) and Osmium(II) Complexes and those of Free
- 929 Ligands. J. Electroanal. Chem. Interfacial Electrochem. 1975, 58, 401–930 410.
- 931 (66) Damrauer, N. H.; McCusker, J. K. Ultrafast Dynamics in the 932 Metal-to-Ligand Charge Transfer Excited-State Evolution of [Ru(4,4'-

- Diphenyl-2,2'-bipyridine) $_3$]²⁺. *J. Phys. Chem. A* **1999**, 103, 8440–933 8446.
- (67) McCusker, J. K. Femtosecond Absorption Spectroscopy of 935 Transition Metal Charge-Transfer Complexes. *Acc. Chem. Res.* **2003**, 936, 876–887.
- (68) Marcaccio, M.; Paolucci, F.; Paradisi, C.; Carano, M.; Roffia, S.; 938 Fontanesi, C.; Yellowlees, L. J.; Serroni, S.; Campagna, S.; Balzani, V. 939 Electrochemistry and Spectroelectrochemistry of ruthenium(II)- 940 Bipyridine Building Blocks. Different Behaviour of the 2,3- and 2,5- 941 bis(2-Pyridyl)pyrazine Bridging Ligands. *J. Electroanal. Chem.* **2002**, 942 532, 99–112.
- (69) Bhasikuttan, A. C.; Suzuki, M.; Nakashima, S.; Okada, T. 944 Ultrafast Fluorescence Detection in Tris(2,2'-bipyridine)ruthenium- 945 (II) Complex in Solution: Relaxation Dynamics Involving Higher 946 Excited States. *J. Am. Chem. Soc.* **2002**, *124*, 8398–8405.
- (70) Yoon, S.; Kukura, P.; Stuart, C. M.; Mathies, R. A. Direct 948 Observation of the Ultrafast Intersystem Crossing in Tris(2,2'- 949 bipyridine)ruthenium(II) Using Femtosecond Stimulated Raman 950 Spectroscopy. *Mol. Phys.* **2006**, *104*, 1275–1282.
- (71) Chen, P.; Omberg, K. M.; Kavaliunas, D. A.; Treadway, J. A.; 952 Palmer, R. A.; Meyer, T. J. Insights on the Excited State Electronic 953 Structures of Ruthenium(II) Polypyridine Complexes Obtained by 954 Step-Scan Fourier Transform Infrared Absorption Difference Time-955 Resolved Spectroscopy. *Inorg. Chem.* 1997, 36, 954–955.
- (72) Hansch, C.; Leo, A.; Taft, R. W. A Survey of Hammett 957 Substituent Constants and Resonance and Field Parameters. *Chem.* 958 *Rev.* 1991, 91, 165–195.